Photoacoustics 19 (2020) 100172

Contents lists available at ScienceDirect

Photoacoustics

journal homepage: www.elsevier.com/locate/pacs

Soft ultrasound priors in optoacoustic reconstruction: Improving clinical vascular imaging

Hong Yang[a,b], Dominik Jüstel[a,b], Jaya Prakash[c], Angelos Karlas[a,b,d], Anne Helfen[e], Max Masthoff[e], Moritz Wildgruber[e,f], Vasilis Ntziachristos[a,b,*]

[a] Institute of Biological and Medical Imaging (IBMI), Helmholtz Zentrum München, Ingolstädter Landstr. 1, D-85764, Neuherberg, Germany
[b] Chair of Biological Imaging and TranslaTUM, Technical University of Munich, Ismaninger Str. 22, 81675, München, Germany
[c] Dept. of Instrumentation and Applied Physics, Indian Institute of Science, C. V. Raman Road, 560012, Bangalore, India
[d] Clinic for Vascular and Endovascular Surgery, Klinikum rechts der Isar, Ismaninger Str. 22, D-81675, München, Germany
[e] Department of Clinical Radiology, University Hospital Muenster, Albert-Schweitzer-Campus 1, A16, 49149, Muenster, Germany
[f] Klinik und Poliklinik für Radiologie, Klinikum der Universität München, Munich, Germany

ARTICLE INFO

Keywords:
Photoacoustics
Hybrid imaging
Regional Laplacian regularization
Carotid
Radial artery

ABSTRACT

Using the same ultrasound detector, hybrid optoacoustic-ultrasound (OPUS) imaging provides concurrent scans of tissue slices or volumes and visualizes complementary sound- and light-based contrast at similar resolutions. In addition to the benefit of hybrid contrast, spatial co-registration enables images from one modality to be employed as prior information for improving an aspect of the performance of the other modality. We consider herein a handheld OPUS system and utilize structural information from ultrasound images to guide regional Laplacian regularization-based reconstruction of optoacoustic images. Using phantoms and data from OPUS scans of human radial and carotid arteries, we show that ultrasound-driven optoacoustic inversion reduces limited-view artefacts and improves image contrast. In phantoms, prior-integrated reconstruction leads to a 50 % higher contrast-to-noise ratio (CNR) of the image than standard reconstruction, and a 17 % higher structural similarity (SSIM) index. In clinical data, prior-integrated reconstruction detects deep-seated radial arteries with higher CNR than the standard method at three different depths. In this way, the prior-integrated method offers unique insights into atherosclerotic carotid plaques in humans (with $p < 0.01$ between patients and healthy volunteers), potentially paving the way for new abilities in vascular imaging and more generally in optoacoustic imaging.

1. Introduction

Handheld optoacoustic (photoacoustic) imaging has recently demonstrated potent clinical imaging abilities in cancer detection [1–4], label-free assessment of tissue inflammation [5,6], tissue metabolism [7] or imaging of vascularization [8–10] or lipids [11,12]. Offering higher resolution than diffuse optical tomography [13,14], optoacoustic imaging is able to resolve morphological structures and to quantify tissue biomarkers, which is not possible using diffuse photons [15]. Moreover, fast wavelength tuning, parallel detection from up to 512 detection channels [15] and advanced spectral unmixing techniques [16], lead to handheld implementations that now demonstrate technological maturity for clinical use.

In analogy to ultrasonography clinical systems, many handheld optoacoustic imaging systems use one-dimensional detector arrays. Such implementations allow the combination of optoacoustic and ultrasound imaging in one hybrid modality. However, this implementation leads to limited-view acoustic detection geometries and the collection of incomplete optoacoustic projection data from the imaged tissue. As a consequence, the corresponding reconstruction problem is ill-posed, possibly deteriorating imaging performance [17]. Limited-view detection results in streak artefacts [18,19] and in a low contrast-to-noise ratio (CNR) [19] in reconstructed optoacoustic images. Combined with a signal-to-noise ratio (SNR) that decreases with increasing imaging depth [20–23] due to light fluence attenuation, limited-view projection optoacoustic tomography may suffer from lowered image quality as a function of depth. Therefore, there is strong motivation to develop methodologies to improve the optoacoustic image quality and

* Corresponding author at: Institute of Biological and Medical Imaging (IBMI), Helmholtz Zentrum München, Ingolstädter Landstr. 1, D-85764, Neuherberg, Germany.
E-mail address: v.ntziachristos@tum.de (V. Ntziachristos).

https://doi.org/10.1016/j.pacs.2020.100172
Received 29 October 2019; Received in revised form 24 February 2020; Accepted 26 February 2020
Available online 10 March 2020

facilitate interpretation of physiological and functional information at increased depths, as required in many clinical studies.

Different methodologies have been suggested to account for the effects of limited-projection optoacoustics. Regularization is a suitable tool to condition ill-posed problems and achieve stable approximate solutions, and various regularization methods have been considered in limited-view optoacoustics, including total variation regularization [24] or wavelet sparsity regularization [25,26]. Hard thresholding, truncated generalized singular value decomposition or preconditioning methods [22] have also been proposed for limited-view optoacoustic tomography. Also, a prefiltering technique has been developed for reducing streak artefacts, based on a full characterization of the artefacts in the framework of microlocal analysis [18]. A Fast Fourier transform-based reconstruction algorithm has been demonstrated to eliminate limited-view artefacts by enclosing the target in a reverberant cavity to generate a periodically repeating acoustic field [19]. However, while regularization and filtering address limited-view acquisition problems in a generic way, they do not use information specific to the sample under investigation and are not sufficient to restore the information that is lost due to incomplete data acquisition.

The relatively straightforward availability of hybrid optoacoustic-ultrasound (OPUS) imaging systems allows for a different approach in improving limited-view optoacoustic imaging. Ultrasound images generally provide anatomical images of tissues and can further resolve blood flow using Doppler techniques. In this role they can be employed post-hoc to aid the interpretation of optoacoustic images [4,27–34]. Special implementations of ultrasound imaging can also be considered, for providing information about acoustic reflections in the sample imaged and for the subsequent correction of reflections from the optoacoustic images [35]. Nevertheless, reduction of acoustic reflections does not address the problem of limited-view projections common in clinical OPUS imaging. Studies involving simulations, phantoms, or *ex vivo* experiments have shown that full-view ultrasound transmission data can be used to estimate the speed of sound distribution in the sample, which in turn can be used to improve the optoacoustic image quality [36,37]. However, due to the requirements of full-view data acquisition, this approach is not applicable to handheld optoacoustic imaging.

Herein we propose a novel approach for utilizing ultrasonography data co-registered with optoacoustic data, i.e. as typically collected from clinical OPUS systems, to improve the limited-view tomographic optoacoustic problem. We hypothesized that the ultrasound information could substantially improve the image quality of reconstructed images and improve medical diagnostics in an adaptive, tissue-specific manner. In particular, we considered a regional Laplacian regularization functional for optoacoustic tomography that incorporates structural information obtained from co-registered ultrasound images. Using simulations and in vivo measurements, we examine whether the proposed use of priors reduces limited-view artefacts and increases the contrast of structures deep in tissue. Then, we apply the method in clinical OPUS carotid imaging data and show the merits of the proposed method compared to stand-alone optoacoustic imaging. We further demonstrate that clinically important functional features of atherosclerotic plaques in the carotid can be observed with a clinical handheld OPUS system.

2. Background

For optoacoustic imaging, the propagation of the acoustic pressure wave $p(\boldsymbol{r}, t)$ at a spatial position $\boldsymbol{r}$ and a time instant t is described by the wave equation [38]:

$$\frac{\partial^2 p(\boldsymbol{r}, t)}{\partial t^2} - c^2 \Delta p(\boldsymbol{r}, t) = \Gamma \frac{\partial H(\boldsymbol{r}, t)}{\partial t}, \tag{1}$$

Where c is the sound speed, Γ is the Grüneisen coefficient, which is assumed to be constant, and $H(\boldsymbol{r}, t)$ is the absorbed energy density. Based on Eq. (1), for pulsed illumination the optoacoustic pressure distribution at $\boldsymbol{r}$ and t in an acoustically homogeneous medium is given by:

$$p(\boldsymbol{r}, t) = \frac{\Gamma}{4\pi c} \frac{\partial}{\partial t} \int_{|\boldsymbol{r}-\boldsymbol{r}'|=ct} \frac{H(\boldsymbol{r}')}{|\boldsymbol{r}-\boldsymbol{r}'|} dl(\boldsymbol{r}'). \tag{2}$$

The initial pressure distribution p_0 at $t = 0$ satisfies $p_0(\boldsymbol{r}) \coloneqq p(\boldsymbol{r}, 0) = \Gamma H(\boldsymbol{r})$ with vanishing time derivative $\frac{\partial}{\partial t} p(\boldsymbol{r}, 0) = 0$, where the time-independence of H is due to negligible duration of the illuminating laser pulse.

Several algorithms have been suggested for the inversion of Eq. (2), i.e., for the reconstruction of p_0 or H, given the optoacoustic signal $p(\boldsymbol{d}, t)$ at the detector locations $\boldsymbol{d}$ [22,39–41]. Among these algorithms, filtered backprojection methods are commonly used due to their simplicity. Nevertheless, images reconstructed with backprojection algorithms suffer from approximation errors, leading to less accurate quantitative functional or molecular imaging [42]. Moreover, backprojection cannot account for the information loss due to limited view. Model-based inversion has been suggested as a more precise and flexible alternative to backprojection [41]. In contrast to backprojection, model-based schemes can explicitly take experimental characteristics into account and offer superior accuracy and image fidelity.

2.1. Model-based optoacoustic reconstruction

Model-based schemes reconstruct optoacoustic images by minimizing the discrepancy between the measured acoustic signals and the signals theoretically predicted by the forward model. Rosenthal et al. [41] developed a semi-analytical model-based scheme, termed interpolated-matrix-model inversion (IMMI), to achieve real-time reconstruction. Discretizing the linear forward model for acoustic wave propagation in Eq. (2) leads to

$$\boldsymbol{p} = \boldsymbol{M}\boldsymbol{x}, \tag{3}$$

Where $\boldsymbol{p}$ stands for the optoacoustic signal; $\boldsymbol{x}$ is the unknown image, i.e., the spatial distribution of energy absorbed per unit volume of the tissue in the imaging plane, written in a vector representation; and $\boldsymbol{M}$ is the model matrix that computes sound propagation in the imaged medium for the experimental acquisition geometry employed. The inversion of Eq. (3) is achieved by minimizing the squared error

$$\boldsymbol{x}_{sol} = \arg\min_{\boldsymbol{x}} \boldsymbol{p}_{det} - \boldsymbol{M}\boldsymbol{x}_2^2 \tag{4}$$

typically using the LSQR algorithm. In Eq. (4), $\boldsymbol{p}_{det}$ is the detected optoacoustic signal and $\|\bullet\|_2$ is the L^2 -norm.

2.2. L^2 regularization

As the minimization problem given in Eq. 4 is ill-posed for limited-view geometry, regularization is required to achieve a unique and stable reconstruction. In addition, a suitable regularization often reduces the noise level and artefacts [22,38]. The most common regularization method is L^2 regularization, i.e. regularization with a functional of the form $\boldsymbol{x} \mapsto \|\boldsymbol{L}\boldsymbol{x}\|_2^2$:

$$\boldsymbol{x}_{sol} = \arg\min_{\boldsymbol{x}} \boldsymbol{p}_{\text{det}} - \boldsymbol{M}\boldsymbol{x}_2^2 + \lambda \boldsymbol{L}\boldsymbol{x}_2^2, \tag{5}$$

Where $\boldsymbol{L}$ is the regularization matrix and $\lambda > 0$ is the regularization parameter. A suitable regularization parameter can, for example, be selected via the L-curve. The L-curve is a plot of the penalty term ($\|\boldsymbol{L}\boldsymbol{x}\|_2$) against the norm of the residual ($\|\boldsymbol{p}_{det} - \boldsymbol{M}\boldsymbol{x}\|_2$). It is a convenient graphical tool for displaying the trade-off between the regularizing functional and the fit to the given data with respect to the regularization parameter. Usually, the optimal trade-off is achieved close to the corner of the L-shaped curve [43].

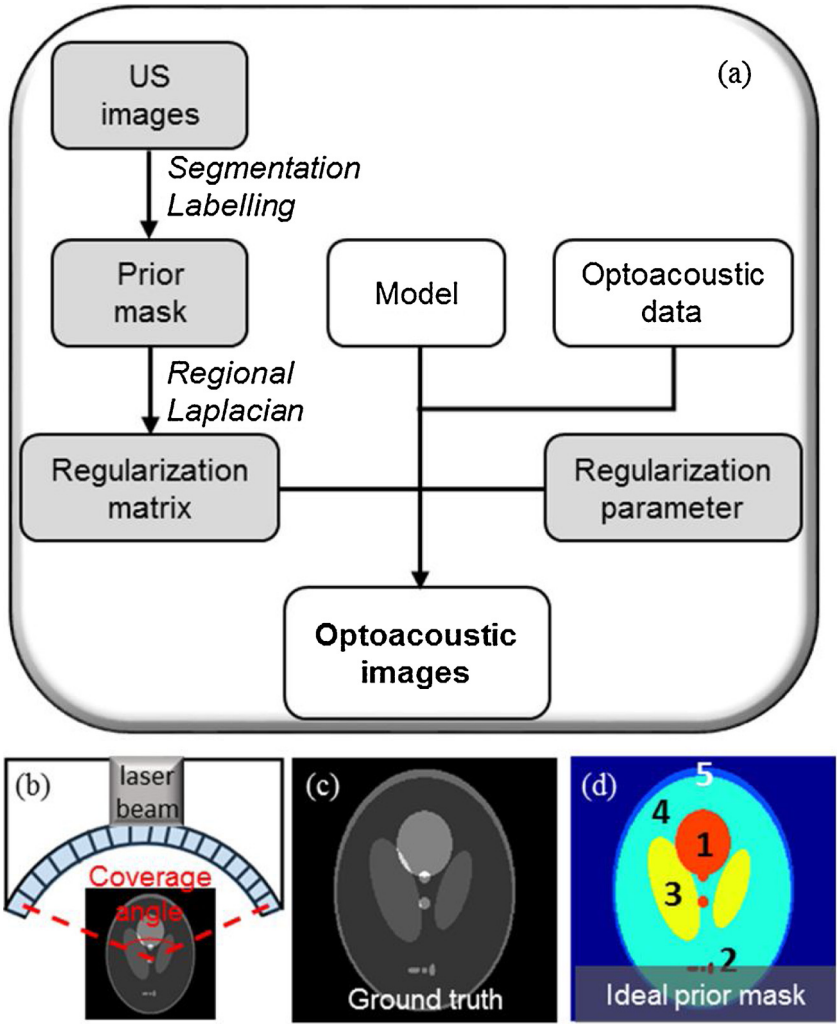

Fig. 1. Block diagram of prior-integrated reconstruction, the related imaging setup and numerical phantom used for simulation. **(a)** Block diagram of prior-integrated reconstruction. **(b)** Imaging set-up, with detectors shown in blue. **(c)** Shepp–Logan phantom without noise (**ground truth**). **(d)** Segmented prior mask with 5 labelled ROIs (**ideal prior mask**).

3. Methods

OPUS systems provide complementary information in co-registered ultrasound and optoacoustic images: ultrasound images provide acoustic contrast to identify regions with different acoustic properties, while optoacoustic images provide optical contrast to identify regions with different optical properties. Since tissues with different acoustic properties usually also differ in optical properties, we designed a regularizer based on ultrasound images that promotes smoothness within regions of constant acoustic properties. To take into account the possibility that tissue features or types may have optical contrast, but no acoustic contrast, the prior needs to be 'soft', in the sense, that it does not sacrifice this pure optical contrast.

In the framework of l^2 regularization, prior spatial knowledge about the reconstructed object can be integrated into the reconstruction by designing a suitable regularization matrix $\boldsymbol{L}$. Previous studies have shown that using the spatial priors in this fashion – as a so-called 'soft prior' [44] – does not bias the image formation when the prior information is imperfect [45]. For example, knowing that the reconstructed object is a smooth function, the matrix $\boldsymbol{L}$ can be chosen to be a spatial high-pass filter, e.g., a discrete Laplacian operator. If, instead, it is known that the reconstructed object is smooth in certain regions and varies strongly in other regions, a regional smoothness prior based on Laplacian method can be incorporated into $\boldsymbol{L}$. Both of these cases will be introduced in the following sections for the special case of OPUS imaging, and their performance will be compared using simulations and clinical datasets.

3.1. Spatial high-pass filter regularization (standard reconstruction)

The matrix $\boldsymbol{L}$ in Eq. 5 can be defined as a spatial derivative operator [22,38,46]. In this case, the regularization term discriminates the high-frequency content of the image [47]. Including such a term into the regularization selects an image that is consistent with the data, while having a minimal amount of high-frequency components. The regularization parameter needs to be chosen such that high-frequency noise is suppressed, while edges are preserved. In the present study, $\boldsymbol{L}$ was defined to be a 2D discrete Laplacian operator given as:

$$L_{ij} = \begin{cases} 1, & \text{if } i = j \\ -\frac{1}{8}, & \text{if } j \in 8 \text{ neighbours of } i. \\ 0, & \text{otherwise} \end{cases} \quad (6)$$

Throughout this paper, least-squares reconstruction with this regularization operator is termed 'standard reconstruction'.

3.2. Regional Laplacian regularization (prior-integrated reconstruction)

Regional Laplacian regularization can be used to integrate prior information obtained by segmenting an ultrasound image of the sample into different tissue types. Similar to previous methods [45,48], we construct an anisotropic non-homogeneous smoothness prior:

$$L_{ij} = \begin{cases} 1, & if\ i = j \\ -\dfrac{1}{N_k - 1}, & if\ i \neq j\ and\ i\ ,\ j\ \in\ ROI_k\ , \\ 0, & otherwise \end{cases} \tag{7}$$

Where k is the index of the region of interest (ROI) and N_k is the number of pixels in ROI_k. The ROIs are obtained by segmenting an ultrasound image into n ROIs labelled by the index $k \in \{1,2,3,\ldots,n\}$. With this design of the L matrix, each ROI is weighted equally, regardless of its area. It is the analogue of the random walk normalized graph Laplacian. Throughout this paper, least-squares reconstruction with this regularization operator is termed 'prior-integrated reconstruction'.

This design of $\boldsymbol{L}$ promotes a reconstructed image that is smooth inside each ROI and highlights the difference between different ROIs, remaining consistent with the data. This approach is based on the idea that dominant photon-absorbers vary between different tissue types, but are similar within one tissue type. Therefore, it is reasonable to expect heterogeneity among different ROIs and homogeneity within one ROI. Fig. 1a shows the workflow to integrate the ultrasound prior into a model-based optoacoustic reconstruction. From the ultrasound images, ROIs are segmented and labelled to form a prior mask. Then the regularization matrix $\boldsymbol{L}$ is constructed based on Eq. (7). Finally, an appropriate regularization parameter is chosen to reconstruct optoacoustic images from the acquired optoacoustic data using the model-based scheme in Eq. (5).

3.3. Numerical simulation

A numerical Shepp-Logan phantom was used to simulate the optoacoustic signals based on Eq. (3), where the model matrix $\boldsymbol{M}$ was calculated based on the probe (Fig. 1b) of the Acuity 256 imaging system (introduced in Section 3.4). In addition, zero mean Gaussian noise was added to achieve a certain SNR. In other words, the simulated optoacoustic signal $\boldsymbol{p}_{sim}$ takes the form:

$$\boldsymbol{p}_{sim} = \boldsymbol{M}(\boldsymbol{x}_{SL} + \varepsilon), \tag{8}$$

Where $\boldsymbol{x}_{SL}$ is the Shepp-Logan phantom without noise (Fig. 1c) and ε is zero mean Gaussian noise. The simulated optoacoustic signals $\boldsymbol{p}_{sim}$ were filtered according to the bandwidth of the transducer and inverted using standard and prior-integrated reconstruction, and the performance of those two methods was assessed based on the reconstructed image quality using the metrics described in Section 3.6. In order to analyze the effect of various parameters on algorithm performance (noise level, coverage angle of the transducer array, segmentation accuracy, ROI labelling, and regularization parameter), we performed multiple simulations by modifying the Shepp-Logan phantom and the ideal prior mask in Fig. 1d, which was segmented from the ground truth image.

The mentioned parameters were analyzed in 4 groups of simulations. In the first group (SIM1), different noise levels and coverage angles of the detector array were simulated; in the second group (SIM2), segmentation errors (e.g. too large or small ROIs), were mimicked with morphological operations; in the third group (SIM3), labelling errors were simulated; and in the fourth group (SIM4), the simulated signals were reconstructed with varying regularization parameters.

3.3.1. Noise and coverage angle (SIM1)

In order to analyze the robustness of the algorithm with respect to noise in the optoacoustic signal, we added different levels of white Gaussian noise ε to degrade the ground truth image $\boldsymbol{x}_{SL}$, achieving an SNR (dB) of 26, 20, 16.5, 14, 12, 10.5, 9.1, 8, 7 and 6 for the simulated optoacoustic signal $\boldsymbol{p}_{sim}$. The ability of the algorithm to deal with the limited-view projections was analyzed by simulating the following coverage angles of the transducers: 200°, 175°, 150°, 125°, 100°, 75° and 50°. Except for this group, for all other simulations the default SNR was 26 dB and coverage angle 125°.

3.3.2. Segmentation accuracy (SIM2)

Accurate image segmentation in the presence of noise is challenging. Therefore, we used morphological operations (i.e. erosion and dilation) to mimic inaccurate segmentation. For the Shepp-Logan phantom, the exact segmented prior mask, termed the 'ideal prior mask', is shown in Fig. 1d. We shrank each region in the ideal prior mask with a disk of diameter 2, 4, 6 or 8 pixels to simulate the case that the ROIs are segmented too small; and we expanded each region in the ideal mask with a disk of diameter 2, 4, 6 or 8 pixels to simulate the case that the ROIs are segmented too large. Another potential segmentation error is the number of segmented regions, as for different segmentation methods, the number of segmented ROIs may vary. In order to analyze how this parameter affects the quality of the reconstructed images, we derived 5 prior masks based on the ideal prior mask. The first prior mask included only ROI 1, the second prior mask included ROI 1 and 2, and so on.

3.3.3. ROI labelling (SIM3)

After image segmentation, labelling the segmented ROIs, is a key step in the regional Laplacian method, since the labelling has a direct effect on N_k in Eq. (7). In order to examine the effect of labelling a non-existing region, which mimics the case that a region is an efficient acoustic reflector but not a good optical absorber, we modified the Shepp-Logan phantom by removing the lowermost structure (Fig. 4a) and labelled an independent non-existing ROI 2 in the prior mask (Fig. 4b). A further variant of labelling is to label multiple ROIs as the same tissue type. To simulate this case, we labelled the non-existing ROI 2 in the ideal prior mask with the same label as ROI 1 (Fig. 4c).

3.3.4. Regularization parameter (SIM4)

For regularization problems, many methods have been developed to optimize the selection of regularization parameter λ. In this study, in order to analyze the effect of the prior mask on the selection of the regularization parameter, we used the L-curve [43] to find a proper λ for each prior mask and examined the reconstructed images with different λ.

3.4. Experimental setup

The imaging system used to collect the clinical data in this study was a hybrid handheld OPUS system (Acuity 256; iThera Medical GmbH, Munich, Germany) modelled after previously developed homemade systems using a concave array geometry and a fast wavelength tuning illumination from 680 nm to 980 nm [49,50]. The detector array of the Acuity 256 system comprised 256 cylindrically focused transducer elements of 4 MHz central frequency (-6 dB) and ≥ 50 % bandwidth (-6 dB). These transducer elements are arranged on a circle of 60 mm radius with 145° angular coverage. For the optoacoustic imaging modality, a 25 mJ pulse (of 10 ns duration) is emitted at a 25 Hz repetition rate to excite the sample. Due to the use of the same transducer array, the optoacoustic and ultrasound images recorded with Acuity 256 can be accurately co-registered if no motion is introduced from outside.

3.5. Tissue imaging of healthy volunteers and patients

Procedures on human subjects were performed after obtaining their

written informed consent. As our target application is clinical vascular imaging, we imaged the distal forearm, where, for example, a longitudinal measurement of radial artery dimensions allows assessment of cardiovascular health [51], and on the carotid artery in the lateral aspect of the neck, which is the principal site of cerebrovascular disease and stroke onset [52]. To image the radial artery, we scanned one healthy volunteer over the ventral side of the distal forearm. To image the carotid, we scanned three healthy volunteers and five patients with diagnosed carotid atherosclerosis over the lateral cervical region of the neck on both sides, i.e. 6 healthy volunteers' datasets and 10 patients' datasets in total. Signal data were not averaged for either modality, and no motion correction was performed because the scanning was real-time.

For prior-integrated reconstruction, a prior mask based on segmented ultrasound images was created as follows. For radial artery datasets, the prior mask was obtained by manually segmenting the radial artery in the ultrasound image. For carotid datasets, the lumen in both patients and healthy volunteers and the plaque in patients' data were manually segmented in the ultrasound image. In addition, a mock plaque region was manually drawn beneath the upper boundary of the lumen in healthy volunteers' datasets in order to serve as a control group. Then the above ROIs were duplicated at the same depth in the background region in order to serve as reference regions. The accuracy of all segmentations was confirmed by clinicians.

For image reconstruction, the radial artery images were reconstructed at the wavelength of 800 nm, which allows detection of both oxygenated and deoxygenated blood since their absorption is similar [53]. For the carotid artery, optoacoustic images were reconstructed at wavelengths of 800 nm to detect both oxygenated and deoxygenated blood, 850 nm to mainly detect oxygenated blood and 930 nm to mainly detect lipids [53].

For the quantitative analysis of the carotid dataset, the mean intensity ratio between the ROI and its corresponding reference region in the background at the same depth is used. Since depth and size of the carotid, as well as the light fluence arriving at the carotid vary between people, it is difficult to compare absolute intensity values across datasets from different people without light fluence correction. Therefore, we considered the mean intensity to reduce the effects of carotid size, and analyzed the mean intensity ratio to minimize the effects of depth and light fluence. Note that the signal in the background is not expected to vanish due to the absorption of chromophores in the tissue surrounding the carotid. Thus, the mean intensity ratio is well-defined and can quantify the difference due to absorbers inside the carotid.

3.6. Image quality evaluation

In this study, we compared standard and prior-integrated reconstruction mainly in terms of several quantitative quality indicators of the reconstructed image, as described below.

3.6.1. CNR

As contrast is the most crucial factor to determine if a region can be differentiated from the background or not, we used CNR to quantify the improvement in image contrast. The CNR of an image was defined as follows [54]:

$$CNR = \frac{contrast}{noise} = \frac{|\mu_1 - \mu_2|}{\sqrt{\sigma_1^2 + \sigma_2^2}}, \tag{9}$$

Where μ_1, μ_2 and σ_1, σ_2 are the means and the standard deviations of, respectively, a given ROI and the background (defined as the whole image except for the ROI).

3.6.2. Structural similarity index (SSIM)

Since limited-view projections introduce deformations of structures, SSIM is an appropriate indicator to quantify the structural accuracy of the reconstructed images. SSIM is commonly used for measuring the similarity between two images based on an initial distortion-free image (ground truth) as reference [55]. It can be calculated as.

$$SSIM(x, y) = \frac{(2\mu_x\mu_y + c_1)(2\sigma_{xy} + c_2)}{(\mu_x^2 + \mu_y^2 + c_1)(\sigma_x^2 + \sigma_y^2 + c_2)}, \tag{10}$$

Where μ_x and σ_x^2 are, respectively, the mean and variance of x, with x representing the reconstructed image. μ_y and σ_y^2 are, respectively, the mean and variance of y, with y being the reference image (ground truth). The variable σ_{xy} is the covariance of x and y, while c_1 and c_2 stabilize division by a weak denominator. The latter two factors are defined as $c_1 = (k_1 L)^2$ and $c_2 = (k_2 L)^2$, where L stands for the dynamic range of the image and $k_1 = 0.01$ and $k_1 = 0.03$ in this study. We kept these values of k_1 and k_2 to be the same as in Ref. [55], facilitating comparison across studies. Although the choice of these two values are somewhat arbitrary, the comparison of the two reconstruction methods based on SSIM values is not sensitive to k_1 and k_2, as we demonstrated in Supplementary Information.

4. Results

To demonstrate the performance of the two regularization schemes introduced in the Methods Section, we performed 4 groups of simulations (SIM1: different noise level and coverage angle; SIM2: segmentation errors; SIM3: labelling errors; and SIM4: varying regularization parameters) and reconstructed 2 groups of clinical datasets – one for radial artery images and one for carotid artery images. The reconstruction results for the numerical phantoms are presented in section 4.1, and the results for the clinical datasets are shown in section 4.2.

4.1. Simulations

Fig. 2 shows the results of SIM1, comparing the proposed method to a standard reconstruction method in the presence of various noise levels and coverage angles. Fig. 2a is a degraded Shepp-Logan phantom resulting in a simulated optoacoustic signal of 26 dB SNR. Fig. 2b and c show, respectively, standard and prior-integrated reconstruction of Fig. 2a under the default coverage angle (125°). In Fig. 2b, the structural deformation due to limited-view detection and the image intensity fluctuation within regions due to noise can be observed. These artefacts are reduced by incorporating priors into the reconstruction (see Fig. 2c). In the reconstructed image using the prior-integrated reconstruction in panel 2c, the boundaries of all regions are correctly recovered and the intensity in each region is more homogeneous than that in panel 2b. Fig. 2d shows the CNR of the reconstructed images for varying SNR of the simulated optoacoustic signal. For linearly decreasing SNR, the CNR of the reconstructed images also decreases linearly. However, the CNR of the prior-integrated reconstructions decreases more slowly than the CNR of the standard reconstructions, while the CNR of the prior-integrated reconstruction outperforms the ones of the standard reconstruction at all SNR levels. At all SNR levels, prior-integrated reconstruction achieves an increase in CNR of at least 50 % relative to the standard reconstruction. Fig. 2e shows the SSIM of the reconstructions for varying coverage angles. With standard reconstruction, the structural similarity of the reconstructed images decreases linearly with decreasing coverage angle. However, with prior-integrated reconstruction, the SSIM of the reconstructed images remains relatively unchanged even when the coverage angle decreases dramatically. Thus prior-integrated reconstruction exhibits SSIM values that are 17–57 % higher than standard reconstruction.

Fig. 3 shows the results of SIM2, which analyzes the effect of segmentation accuracy on prior-integrated reconstruction with respect to the size and number of the segmented ROIs. Fig. 3a shows an inaccurately segmented prior mask. Fig. 3b shows the reconstruction

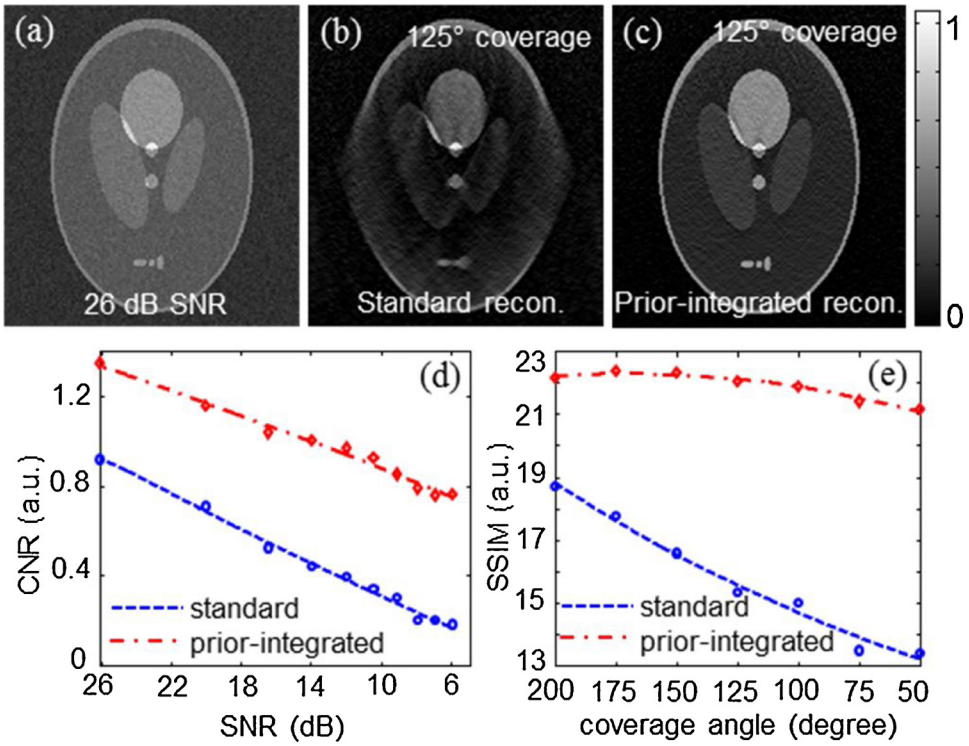

Fig. 2. Reconstruction of the Shepp-Logan phantom using standard and prior-integrated reconstruction for different noise levels and coverage angles. The ground truth image is shown in Fig. 1c; the prior mask is shown in Fig. 1d. **(a)** Shepp–Logan phantom with zero-mean Gaussian noise (26 dB SNR). **(b-c)** Reconstructed image under a 125° coverage angle with (b) standard or (c) prior-integrated reconstruction. **(d)** CNR of the reconstructed images at different noise levels following standard (dashed blue) or prior-integrated (dash-dotted red) reconstruction. **(e)** Variation of SSIM of the reconstructed images with respect to the coverage angle.

result of the degraded phantom (Fig. 2a) using the prior mask in Fig. 3a. On this image, the true boundary of each ROI remains while the prior mask introduces false boundaries inside each ROI, which is expected to be reflected by a lower SSIM index. Fig. 3c shows the SSIM in the presence of various segmentation errors. When there is no segmentation error or when the segmented ROI is slightly larger than the ground truth, the SSIM of the reconstructed images with prior-integrated reconstruction is optimal. However, if the segmented ROI is much smaller or larger than the ground truth (by more than 8 pixels in our simulations), strong false boundaries start to appear in the reconstructed images, reducing the SSIM values. Fig. 3d shows another type of inaccurate prior mask that includes only two ROIs. Fig. 3e presents the reconstruction result of Fig. 2a using the prior mask in Fig. 3d. Due to the prior mask, the structure and intensity of ROI 1 and 2 are well recovered, while the remainder of the image is poorly reconstructed. Fig. 3f shows the variation in CNR for ROI 1 as the number of ROIs in the prior mask changes: more ROIs in the prior mask translates to better CNR. Regardless of the number of ROIs in the segmented prior mask, CNR is always better with prior-integrated reconstruction than with standard reconstruction.

Next, we examine the effects of ROI labelling on prior-integrated reconstruction (SIM3). Fig. 4a is the modified Shepp-Logan phantom,

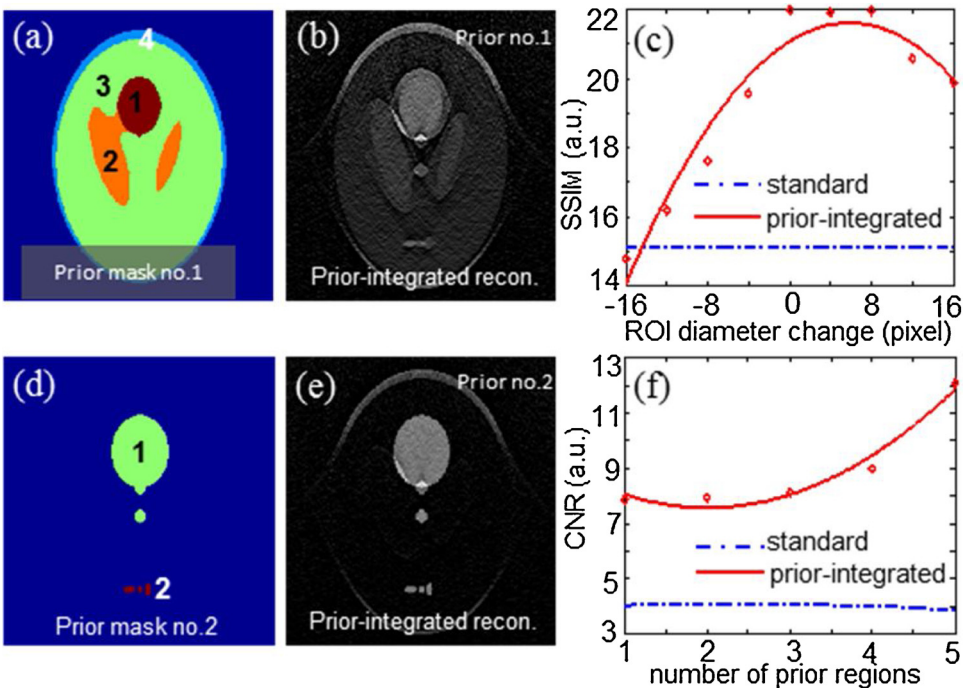

Fig. 3. Effects of segmentation accuracy and the number of ROIs on prior-integrated reconstruction. The ground truth image is shown in Fig. 1c. **(a)** An inaccurately segmented prior mask, which is generated by the erosion of the ideal prior mask in Fig. 1d with a disk of diameter 6 pixels. **(b)** Reconstruction of the noisy phantom (Fig. 2a) using the prior mask in panel (a). **(c)** Variation of SSIM of the reconstructed images with respect to erosion and dilation. **(d)** A prior mask with only 2 ROIs. **(e)** Reconstruction of the noisy phantom in Fig. 2a using the prior mask in panel (d). **(f)** Variation of the CNR of ROI 1 with respect to the number of ROIs. ROIs were added according to their labels in Fig. 1d.

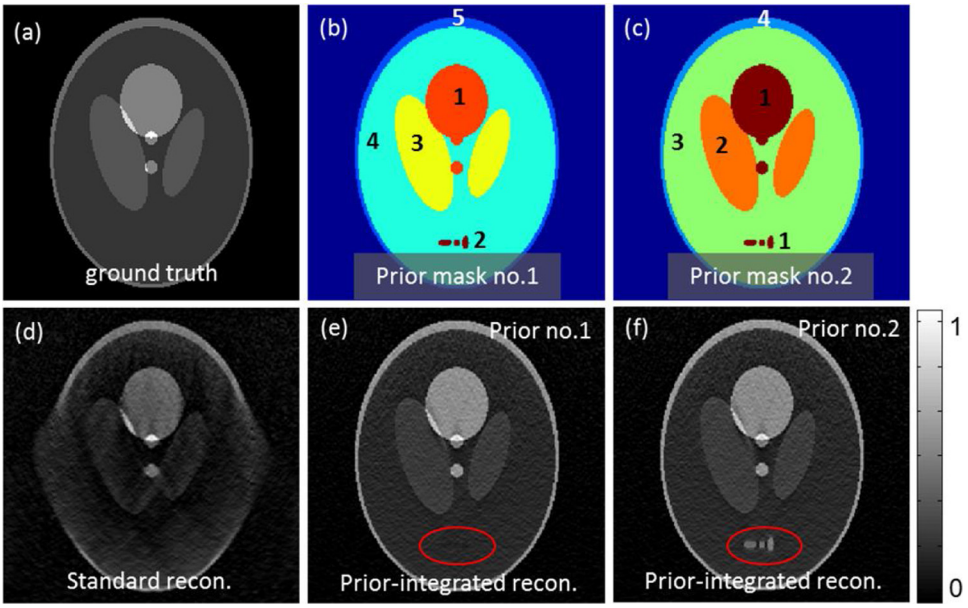

Fig. 4. Effect of ROI labelling on prior-integrated reconstruction. **(a)** A modified Shepp-Logan phantom with the lowermost structure removed. **(b-c)** Inaccurate prior masks in which (b) a nonexistent ROI has been added, or (c) the nonexistent ROI has been added to ROI 1. **(d-f)** Reconstruction of the noisy phantom with (d) standard reconstruction or with prior-integrated reconstruction using (e) prior mask no. 1 or (f) prior mask no. 2. The red ellipse in panels (e) and (f) indicates the location of the ROI that was assigned different labels, introducing a false positive in panel (f).

which was the ground truth in this simulation. Fig. 4b shows an erroneous mask in which a nonexistent region is labelled as ROI 2. Fig. 4c shows that a nonexistent region is labelled as the same tissue type as ROI 1. Fig. 4d is the reconstructed image using standard reconstruction. Fig. 4e is the reconstruction result of prior-integrated reconstruction using the prior mask in Fig. 4b, which shows that the independently labelled ROI 2 does not create a false positive result in the reconstructed image. Fig. 4f shows the prior-integrated reconstruction result with the prior mask on panel 4c, in which a false positive result is created. The labelling of the same non-existing region in panels 4b (own label) and 4c (same label as region 1) gives different results in panels 4e and 4f, illustrating that labelling unconnected regions independently as in panel 4b leads to a correct reconstruction, based on the ground truth in panel 4a.

Since the regularization parameter is important for all regularization methods, SIM4 was performed. Fig. 5 shows the influence of the prior mask and different regularization parameters λ on prior-integrated reconstruction. Fig. 5a is the ideal prior mask, while Fig. 5b shows a prior mask with only one ROI. The latter mask is used for the reconstructions in Fig. 5d-f. Fig. 5c presents the L-curves corresponding to the prior-integrated reconstructions with the masks in panels 5a and 5b. The different corner points of L-curves indicate that, in order to achieve optimal trade-off, optimal regularization parameter needs to be chosen accordingly for different prior masks. Fig. 5d–f show the reconstructed images of Fig. 2a using the prior mask in panel 5b with a small, appropriate or large λ. With a small regularization parameter, the prior-integrated reconstruction is similar to the standard reconstruction. With an appropriate regularization parameter, the ROI can be reconstructed with higher accuracy and maintain the information on the background in prior-integrated reconstruction. With a large regularization parameter, however, the prior dominates the reconstruction result and basically only the prior mask is reconstructed with all other information being discarded.

4.2. Clinical datasets

Based on the simulation results, we proceeded to test the performance of the prior-integrated method for reconstruction of clinical

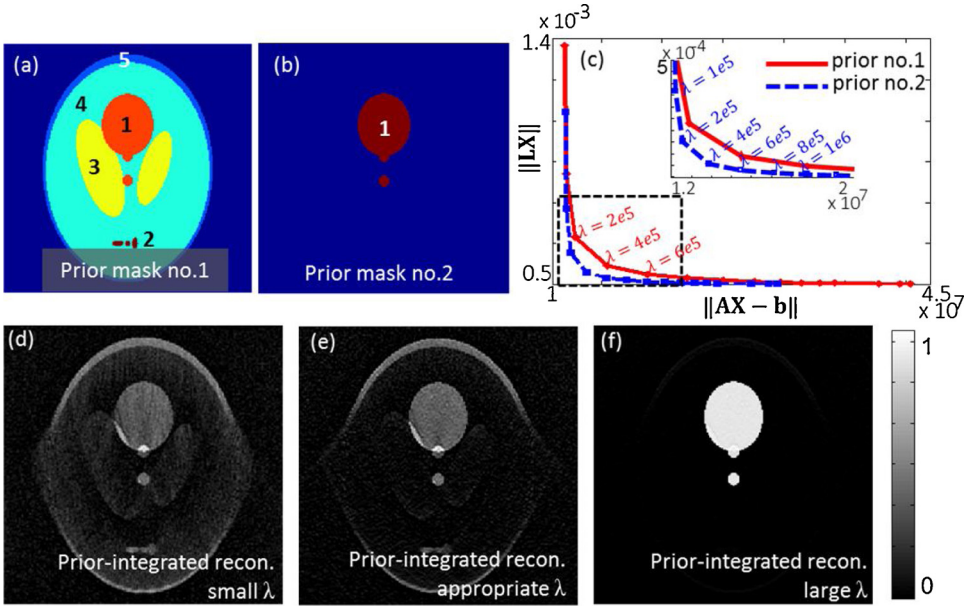

Fig. 5. Effect of the prior mask and the regularization parameter on reconstructed images. The ground truth image is shown in Fig. 1c. **(a)** Ideal prior mask. **(b)** A prior mask that has only ROI 1. **(c)** L-curves corresponding to the prior masks in panels (a) and (b). The inset is enlarged area from the dashed box. **(d-f)** Reconstructions of the noisy phantom in Fig. 2a with the prior mask in panel (b) using **(d)** a small regularization parameter (1e5), **(e)** an appropriate regularization parameter (4e5) or **(f)** a large regularization parameter (1e7).

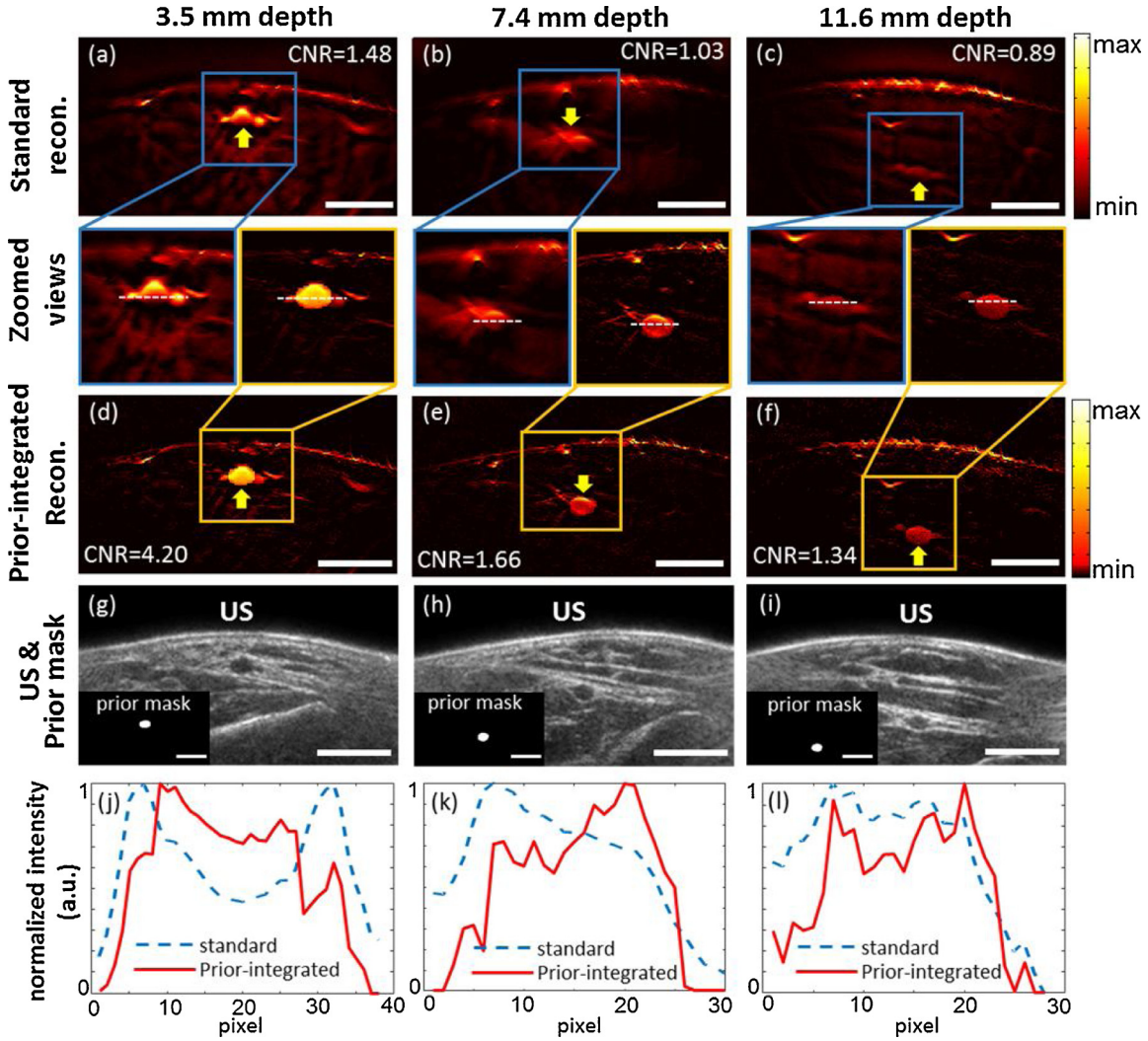

Fig. 6. Reconstruction of the radial artery at different depths using standard and prior-integrated reconstruction. Standard reconstruction of the radial artery at 800 nm at depths of **(a)** 3.5 mm, **(b)** 7.4 mm and **(c)** 11.6 mm. Prior-integrated reconstruction of the radial artery at 800 nm at depths of **(d)** 3.5 mm, **(e)** 7.4 mm and **(f)** 11.6 mm. Ultrasound images of the radial artery at depths of **(g)** 3.5 mm, **(h)** 7.4 mm and **(i)** 11.6 mm, and the corresponding prior masks used in prior-integrated reconstruction. The line profiles of the radial artery along the white doted lines in the zoomed views at depths of **(j)** 3.5 mm, **(k)** 7.4 mm and **(l)** 11.6 mm. The scale bar is 1 cm.

datasets. Fig. 6 shows the reconstruction results for radial arteries at different depths using both the standard and prior-integrated reconstruction. Fig. 6a–c show the standard reconstruction results of the radial artery at 3.5 mm, 7.4 mm and 11.6 mm depth, respectively. The contrast and sharpness of the boundaries of radial artery (marked with yellow arrow in each panel) is decreasing along depth. Fig. 6d–f show the reconstructed images of the radial artery using the prior-integrated reconstruction at a depth of 3.5 mm, 7.4 mm and 11.6 mm, respectively. In all three images, a clear boundary of the radial artery is recovered, and the intensity of the radial artery region is higher than that of the surrounding tissue. In the zoomed-in images, prior-integrated reconstruction gives better contrast and structural integrity for the radial artery than standard reconstruction at all depths. Fig. 6g-i are the ultrasound images and the segmented prior masks for the radial arteries at three depths. Fig. 6j–l are the line profiles of the radial arteries along the white dashed line in the zoomed-in views corresponding to the two reconstruction methods at different depths. With standard reconstruction, the relative intensity difference between radial artery and background decreases with depth from panel 6 j to panel 6 l, while the prior-integrated reconstruction maintains a similar difference/sharp edges at all depths demonstrating the improved CNR over standard reconstruction.

Fig. 7 compares the performance of prior-integrated and standard reconstruction for reconstructing images of the carotid artery of an atherosclerosis patient and of a healthy individual. In this figure, gamma correction and a rolling ball background subtraction [56] have been applied to the optoacoustic images to achieve the best visualization of the carotid region in each image. Therefore, the displayed intensity is not quantitative and cannot be compared across panels. Fig. 7a–i are the results of patients diagnosed with carotid atherosclerosis. Fig. 7a is the prior mask used for reconstructing the carotid at 850 nm. Fig. 7b is the reconstructed optoacoustic image at 850 nm using the prior mask in panel 7a. Fig. 7c is the reconstructed image at 850 nm using the standard reconstruction. Comparing Fig. 7b and c, the carotid is difficult to distinguish from the background in the standard reconstruction, but it is visible in the prior-integrated reconstruction. Fig. 7d-f show the reconstructed optoacoustic images at 930 nm with prior-integrated reconstruction and standard reconstruction, respectively. With the standard reconstruction, the plaque in the carotid artery is not recognizable from the optoacoustic images, but the lesion is detectable in Fig. 7e. Fig. 7g is the co-registered ultrasound image from which the prior masks are segmented; the lumen of carotid artery is highlighted using a dashed red ellipse. Fig. 7h is the overlay of US and the optoacoustic images of panels 7b and 7e. Fig. 7i is the overlay of the

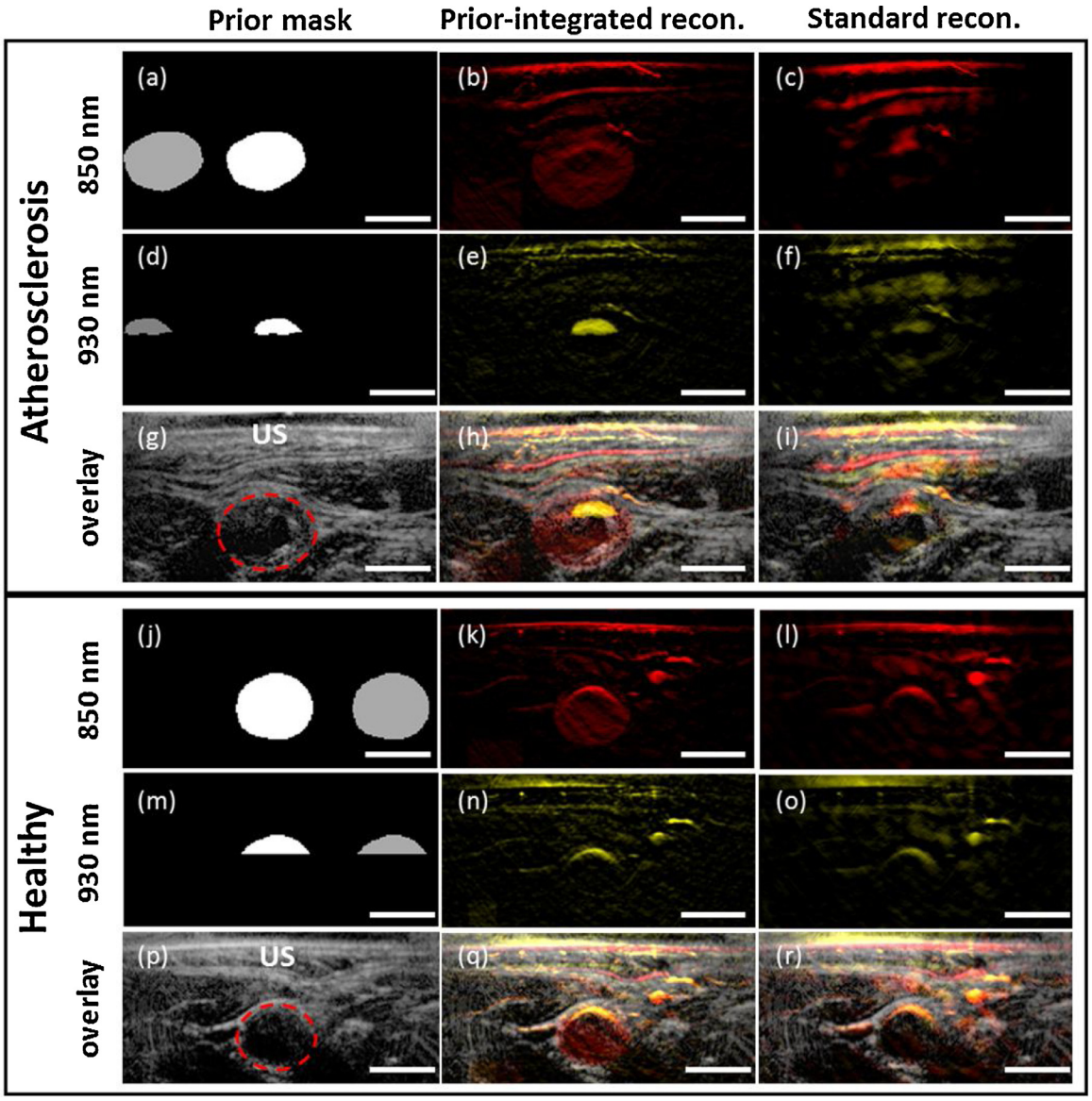

Fig. 7. Standard and prior-integrated reconstruction of the carotid artery of an atherosclerotic patient (a-i) and of a healthy individual (j-r). **(a)** A prior mask for the carotid. The grey regions in the prior masks are the reference region/control for the true ROI shown in white, the same as those in panel d, j, and m. **(b-c)** Reconstructed images at 850 nm using (b) prior-integrated and (c) standard reconstruction. (d) A prior mask for the lesion inside the carotid. **(e-f)** Reconstructed images at 930 nm using (e) prior-integrated and (f) standard reconstruction. **(g)** US image of the neck region with artery lumen highlighted with the dashed red ellipse, the same as that in panel p. **(h)** Overlay of panels (b), (e) and (g). **(i)** Overlay of panels (c), (f) and (g). **(j-r)** The results of a healthy volunteer are shown in panel. (j) A prior mask of the carotid. **(k-l)** Reconstructed images at 850 nm using (k) prior-integrated and (l) standard reconstruction. (m) Prior mask of a nonexistent lesion inside the carotid. **(n-o)** Reconstructed images at 930 nm using (n) prior-integrated and (o) standard reconstruction. **(p)** US image of the neck region. **(q)** Overlay of panels (k), (n) and (p). **(r)** Overlay of panels (l), (o) and (p). The scale bar is 1 cm.

US and the optoacoustic images of panels 7c and 7f.

Fig. 7j–r are the results of a healthy volunteer as the control. Fig. 7j is the prior mask at 850 nm. Fig. 7k – l are the reconstructed optoacoustic images at 850 nm using the prior mask in panel 7 j and the standard reconstruction, respectively. In those two images, the carotid is well recovered by the prior-integrated method, whereas only the upper boundary is visible with standard reconstruction. Fig. 7m is a manually drawn prior mask including a non-existing lesion and used for the reconstruction at 930 nm to examine whether it introduces a false positive or not. Fig. 7n and o are the reconstructed optoacoustic images at 930 nm with prior-integrated reconstruction and standard reconstruction, respectively. The two reconstruction methods give similar images; the prior-integrated method does not introduce false positive results. Fig. 7p is the co-registered US image from which the prior mask in panel 7 j is segmented. Fig. 7q is the overlay of panel 7p and the optoacoustic images on panel 7k and 7n. Fig. 7r is the overlay of the 7p and the optoacoustic images of panel 7 l and 7o.

Finally, Fig. 8 shows the intensity analysis of 10 datasets from patients and 6 datasets from healthy individuals. The *y*-axis is the mean intensity ratio of the target ROI and the reference region (white region and grey region in the prior masks in Fig. 7, respectively). Fig. 8a–b show that at 800 nm, both prior-integrated and standard reconstruction give a similar intensity ratio for patients and healthy volunteers. This is expected since the image intensity from the target ROI (i.e. lumen) at 800 nm is due mainly to blood absorption in the carotid; hence, there should be no significant difference between atherosclerotic patients and healthy volunteers. In Fig. 8c, prior-integrated reconstruction shows a significant difference ($p < 0.01$) between the patients and healthy volunteers. This is expected, since, in contrast to healthy volunteers, patients with carotid artery disease frequently have atherosclerotic

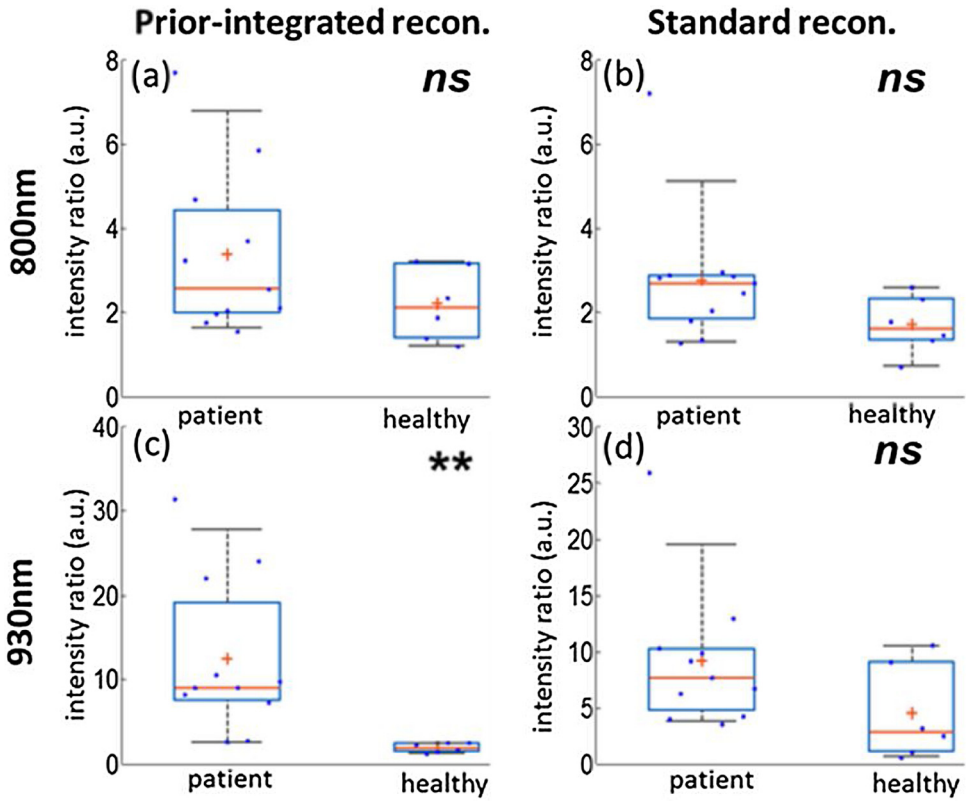

Fig. 8. Statistical analysis of carotid images from atherosclerosis patients and healthy volunteers, using mean intensity ratio of the target ROI and the reference region. **(a-b)** Intensity ratio of the reconstructed images at 800 nm using (a) prior-integrated or (b) standard reconstruction. **(c-d)** Intensity ratio of the reconstructed images at 930 nm using (c) prior-integrated reconstruction and (d) standard reconstruction. ns: difference between two groups is not significant, $p > 0.05$; **: difference between two groups is very significant, $p < 0.01$.

plaques that contain lipids, and lipids are the main absorbers at 930 nm. In Fig. 8d, the standard reconstruction gives similar intensity ratios for patients and healthy individuals at 930 nm. In Fig. 8c and d, a difference in the intensity ratio distribution is observed, depending on whether the reconstruction incorporates US priors or not.

5. Discussion

In this study, we introduced a regional Laplacian method to integrate structural information from ultrasound images as soft priors into optoacoustic reconstruction. The proposed prior-integrated method was characterized with simulations and applied to experimental data in comparison with a standard reconstruction method. The results indicated higher CNR values from prior-integrated reconstruction than from standard one. A higher contrast improves detectability of radial artery with increasing depth, as well as the lumen and plaque in human carotid datasets. Moreover, the prior-integrated reconstruction successfully recovered boundaries subject to limited-view artefacts and thus showed higher SSIM values compared to the standard reconstruction. Further analysis indicated that the proposed prior-integrated reconstruction method stayed robust to decreasing angles of detection, proving an efficient way to at least partially compensate for the information loss due to limited-view detection.

Vertical structures with acoustic contrast can only partially be recovered, which is known to be a major challenge for limited-view geometry optoacoustic systems [21]. The prior-integrated method can use structural information in ultrasound images to compensate for the information loss due to limited-view detection in optoacoustic reconstruction. It is particularly helpful when the ultrasound image possesses good structural integrity even under limited-view detection, which is often true for tissue imaging. Limited-view issues exist in ultrasound imaging, but it does not affect the integrity of structures in ultrasound images as strongly as it does in optoacoustic images. For example, dense scatterers in the tissue surrounding a blood vessel might result in positive contrast in the ultrasound image, compared to the negative contrast of the blood vessel. As a result, even the vertical edges of the vessel boundary can be sharply reconstructed, which is not possible in limited-view optoacoustic imaging due to a lack of optical contrast in the surrounding tissue.

Our quantitative analysis of the carotid datasets in Fig. 8 revealed a significant difference in the mean optoacoustic image intensity ratio at 930 nm in the upper part of the carotid lumen of patients and volunteers when using the proposed prior-integrated reconstruction, while the standard reconstruction did not give a significant difference. This illustrates the potential of the proposed method to increase the capability of functional information extraction, and thus clinical value, of optoacoustic images. This analysis is based on the assumption that similar light energy arrives at similar depths. This assumption might not always be satisfied. For example, if large, heterogeneous absorbers exist along the propagation path of light, the light energy arriving at the lumen may be much less than in the reference region. In such cases, light fluence correction is necessary. Light fluence correction is essential when one aims to unmix lipid in carotid plaque using spectral decomposition, because the proposed prior-integrated method cannot compensate light fluence or the spectral coloring effect. Therefore, without light fluence correction, the proposed prior-integrated method is not expected to outperform the standard reconstruction in spectral decomposition.

Similar regional Laplacian methods have been applied to integrate prior information in multi-modal imaging in other fields, such as in positron emission tomography (PET)-computed tomography [57], PET-magnetic resonance imaging (MRI) [58], fluorescence molecular tomography-x-ray computed tomography [59,60], or diffuse optical tomography (DOT)-MRI [61]. While in these cases, priors are taken from a higher resolution modality and integrated into a lower resolution modality, we demonstrate for the first time that priors from one modality can improve the reconstruction in a second modality when the two modalities offer similar resolution, as is the case for OPUS systems.

Previous studies integrating prior information did not examine how their methods performed with respect to specific isolated factors that

can affect reconstruction quality. Here, we analyzed the influence of three important variables on the reconstruction quality, namely, segmentation accuracy, labelling, and the regularization parameter. False boundaries are observed due to improper segmentation, which implies the necessity of high-quality segmentation to benefit from the proposed method. In case of high segmentation uncertainty, errors can be avoided by only sparsely segmenting target regions and treating the remaining image as background. We demonstrated that the proposed method is sensitive to labelling: adding a non-existing region can introduce false positive features in the reconstructed image, depending on how the region is labelled. In order to avoid such false positives, the labelling of the prior mask is recommended to follow the connectivity of the regions, i.e. two unconnected regions should not be labelled as the same tissue type. The L-curves shown in Fig. 5 demonstrated that different prior masks require different regularization parameters. Since the optoacoustic signals are the key data, the regularization parameter needs to be properly chosen to optimize the trade-off between data fidelity and prior information.

For further improvement of the proposed method, the morphologic mismatch for the same target in ultrasound and optoacoustic images due to the different effective slice thickness should be considered. The difference of the slice thickness could be compensated in two ways. The first way is to increase ultrasound effective slice thickness. One can predefine the thickness of optoacoustic slice by experiments, then scan multiple ultrasound images within the pre-defined thickness. The ultrasound image that is of the same slice thickness as optoacoustic image can then be obtained by summing up all the ultrasound images in that volume. To generate the prior mask, the segmentation is applied to the summed-up ultrasound image. A second way could be to reduce the effective slice thickness of optoacoustic image. By incorporating a 3D sensitivity field of the transducer into the optoacoustic reconstruction model, one can simulate the round-way focusing effect which happens in reflection-mode ultrasound imaging. In such ways, the difference of optoacoustic and ultrasound slice thickness might be minimized and the prior-inaccuracy induced artefacts in optoacoustic images could be reduced. In addition, automatic segmentation of the prior mask could be considered. For example, superpixel segmentation might be an appropriate way to automatically segment the priors. Even though superpixels might over-segment the image, it is expected to find the relevant edges in the ultrasound image [62]. In general, automatic segmentation should avoid the bias introduced by manual segmentation. Also, automatic selection of the regularization parameter should be considered, since using the L-curve is a time-consuming method [63]. Concerning a regularizer that promotes smoothness (instead of uniformity) in the regions directly, we note that, while it is easy to, for example, simply restrict the Laplacian to the inner part of a region, the boundary is problematic. Since the boundary is the central source of information that we input, non-smoothness needs to be properly penalized until the boundary, but not across it. For that purpose, one would need to extract the tangential directions at the whole boundary and engineer suitable directional high-pass filters along it. Such an approach would substantially reduce the computational speed of the method, compromising our idea of a simple and efficient ultrasound prior.

6. Conclusion

In summary, this paper proposes a novel perspective to further enhance the capabilities of handheld OPUS imaging systems. Simultaneous recording of co-registered ultrasound and optoacoustic images using a hybrid handheld system offers not only a comprehensive anatomical ultrasound-based validation of optoacoustic images, but also prior information valuable for improving optoacoustic reconstructions. Ultrasound priors can be efficiently incorporated into optoacoustic model-based reconstruction by a regional Laplacian regularization method based on segmented ultrasound images. This prior-integrated reconstruction is shown to enhance the contrast (as quantified by CNR), reduce limited-view artefacts (as quantified by SSIM) and increase the detectability of structures in deep tissue in clinical optoacoustic images. The demonstrated improvements will allow more accurate image analysis in applications requiring high contrast deep in tissue, such as vascular imaging, and vascularity analysis of soft-tissue tumors. Moreover, by achieving higher contrast in the target ROIs, our method shows great potential for increasing the diagnostic information available to clinicians to support diagnosis, characterization and monitoring of disease and response to therapy.

Declaration of Competing Interest

None.

Acknowledgments

This project has received funding from the European Research Council (ERC) under the European Union's Horizon 2020 research and innovation programme under grant agreement No 694968 (PREMSOT) and from the Deutsche Forschungsgemeinschaft DFG, Germany [Gottfried Wilhelm Leibniz Prize 2013; NT 3/10-1 and as part of the CRC 1123 Z1]. H. Yang acknowledges the support of a CSC fellowship CSC No. 201506960010. Jaya Prakash acknowledges Alexander von Humboldt Postdoctoral Fellowship program.

We thank Dr. A. Chapin Rodríguez, Yuanhui Huang, and Dr. Niklas Markwardt for helpful suggestions on the manuscript.

Appendix A. Supplementary data

Supplementary material related to this article can be found, in the online version, at doi:https://doi.org/10.1016/j.pacs.2020.100172.

References

[1] I. Stoffels, S. Morscher, I. Helfrich, U. Hillen, J. Leyh, N.C. Burton, T.C. Sardella, J. Claussen, T.D. Poeppel, H.S. Bachmann, Metastatic status of sentinel lymph nodes in melanoma determined noninvasively with multispectral optoacoustic imaging, Sci. Transl. Med. 7 (317) (2015) pp. 317ra199.

[2] K.S. Valluru, J.K. Willmann, Clinical photoacoustic imaging of cancer, Ultrasonography 35 (4) (2016) 267.

[3] K.S. Valluru, K.E. Wilson, J.K. Willmann, Photoacoustic Imaging in oncology: translational preclinical and early clinical experience, Radiology 280 (2) (2016) 332–349.

[4] A. Garcia-Uribe, T.N. Erpelding, A. Krumholz, H. Ke, K. Maslov, C. Appleton, J.A. Margenthaler, L.V. Wang, Dual-modality photoacoustic and ultrasound imaging system for noninvasive sentinel lymph node detection in patients with breast cancer, Sci. Rep. 5 (2015) 15748.

[5] F. Knieling, C. Neufert, A. Hartmann, J. Claussen, A. Urich, C. Egger, M. Vetter, S. Fischer, L. Pfeifer, A. Hagel, Multispectral optoacoustic tomography for assessment of Crohn's disease activity, N. Engl. J. Med. 2017 (376) (2017) 1292–1294.

[6] J. Jo, G. Xu, M. Cao, A. Marquardt, S. Francis, G. Gandikota, X. Wang, A functional study of human inflammatory arthritis using photoacoustic imaging, Sci. Rep. 7 (1) (2017) 15026.

[7] J. Reber, M. Willershäuser, A. Karlas, K. Paul-Yuan, G. Diot, D. Franz, T. Fromme, S.V. Ovsepian, N. Bézière, E. Dubikovskaya, Non-invasive measurement of brown fat metabolism based on optoacoustic imaging of hemoglobin gradients, Cell Metab. 27 (3) (2018) 689–701 e4.

[8] A. Taruttis, A.C. Timmermans, P.C. Wouters, M. Kacprowicz, G.M. van Dam, V. Ntziachristos, Optoacoustic imaging of human vasculature: feasibility by using a handheld probe, Radiology 281 (1) (2016) 256–263.

[9] M. Toi, Y. Asao, Y. Matsumoto, H. Sekiguchi, A. Yoshikawa, M. Takada, M. Kataoka, T. Endo, N. Kawaguchi-Sakita, M. Kawashima, Visualization of tumor-related blood vessels in human breast by photoacoustic imaging system with a hemispherical detector array, Sci. Rep. 7 (2017) 41970.

[10] W. Xia, E. Maneas, D.I. Nikitichev, C.A. Mosse, G.S. Dos Santos, T. Vercauteren, A.L. David, J. Deprest, S. Ourselin, P.C. Beard, Interventional photoacoustic imaging of the human placenta with ultrasonic tracking for minimally invasive fetal surgeries, International Conference on Medical Image Computing and Computer-Assisted Intervention, Munich, Germany (2015) 371–378.

[11] T.J. Allen, P.C. Beard, A. Hall, A.P. Dhillon, J.S. Owen, Spectroscopic photoacoustic imaging of lipid-rich plaques in the human aorta in the 740 to 1400 nm wavelength range, J. Biomed. Opt. 17 (6) (2012) pp. 061209.

[12] J.A. Guggenheim, T.J. Allen, A. Plumb, E.Z. Zhang, M. Rodriguez-Justo, S. Punwani, P.C. Beard, Photoacoustic imaging of human lymph nodes with endogenous lipid and hemoglobin contrast, J. Biomed. Opt. 20 (5) (2015) pp. 050504.

[13] L.V. Wang, H.-i. Wu, Biomedical Optics: Principles and Imaging, John Wiley & Sons, 2012.
[14] J. Weber, P.C. Beard, S.E. Bohndiek, Contrast agents for molecular photoacoustic imaging, Nat. Methods 13 (2016) 639 07/28/online.
[15] A. Taruttis, V. Ntziachristos, Advances in real-time multispectral optoacoustic imaging and its applications, Nat. Photonics 9 (4) (2015) 219.
[16] S. Tzoumas, A. Nunes, I. Olefir, S. Stangl, P. Symvoulidis, S. Glasl, C. Bayer, G. Multhoff, V. Ntziachristos, Eigenspectra optoacoustic tomography achieves quantitative blood oxygenation imaging deep in tissues, Nat. Commun. 7 (2016) pp. ncomms12121.
[17] A. Rosenthal, V. Ntziachristos, D. Razansky, Acoustic inversion in optoacoustic tomography: a review, Curr. Med. Imaging Rev. 9 (4) (2013) 318.
[18] J.R. Frikel, E.T. Quinto, Artifacts in incomplete data tomography with applications to photoacoustic tomography and sonar, SIAM J. Appl. Math. 75 (2) (2015) 703–725.
[19] B.T. Cox, S.R. Arridge, P.C. Beard, Photoacoustic tomography with a limited-aperture planar sensor and a reverberant cavity, Inverse Probl. 23 (6) (2007) S95.
[20] X.L. Deán-Ben, D. Razansky, On the link between the speckle free nature of optoacoustics and visibility of structures in limited-view tomography, Photoacoustics 4 (4) (2016) 133–140.
[21] Y. Xu, L.V. Wang, G. Ambartsoumian, P. Kuchment, Reconstructions in limited-view thermoacoustic tomography, Med. Phys. 31 (4) (2004) 724–733.
[22] A. Buehler, A. Rosenthal, T. Jetzfellner, A. Dima, D. Razansky, V. Ntziachristos, Model-based optoacoustic inversions with incomplete projection data, Med. Phys. 38 (3) (2011) 1694–1704.
[23] W. Dan, T. Chao, L. Xiao-Jun, W. Xue-Ding, Influence of limited-view scanning on depth imaging of photoacoustic tomography, Chinese Phys. B 21 (1) (2012) pp. 014301.
[24] L. Yao, H. Jiang, Photoacoustic image reconstruction from few-detector and limited-angle data, Biomed. Opt. Express 2 (9) (2011) 2649–2654.
[25] J. Frikel, M. Haltmeier, Efficient regularization with wavelet sparsity constraints in PAT, arXiv preprint (2017) arXiv:1703.08240.
[26] A. Rosenthal, T. Jetzfellner, D. Razansky, V. Ntziachristos, Efficient framework for model-based tomographic image reconstruction using wavelet packets, IEEE Trans. Med. Imaging 31 (7) (2012) 1346–1357.
[27] J. Kim, S. Park, Y. Jung, S. Chang, J. Park, Y. Zhang, J.F. Lovell, C. Kim, Programmable real-time clinical photoacoustic and ultrasound imaging system, Sci. Rep. 6 (2016).
[28] K. Sivasubramanian, M. Pramanik, High frame rate photoacoustic imaging at 7000 frames per second using clinical ultrasound system, Biomed. Opt. Express 7 (2) (2016) 312–323.
[29] C. Kim, T.N. Erpelding, L. Jankovic, L.V. Wang, Performance benchmarks of an array-based hand-held photoacoustic probe adapted from a clinical ultrasound system for non-invasive sentinel lymph node imaging, Philosophical Transactions of the Royal Society of London A: Mathematical, Physical and Engineering Sciences 369 (1955) (2011) 4644–4650.
[30] C.-W. Wei, T.-M. Nguyen, J. Xia, B. Arnal, E.Y. Wong, I.M. Pelivanov, M. O'Donnell, Real-time integrated photoacoustic and ultrasound (PAUS) imaging system to guide interventional procedures: ex vivo study, IEEE Trans. Ultrason. Ferroelectr. Freq. Control 62 (2) (2015) 319–328.
[31] M.K.A. Singh, W. Steenbergen, S. Manohar, Handheld probe-based dual mode ultrasound/photoacoustics for biomedical imaging, Frontiers in Biophotonics for Translational Medicine (2016) 209–247 Springer.
[32] J. Jo, G. Xu, A. Marquardt, G. Girish, and X. Wang, "Photoacoustic evaluation of human inflammatory arthritis in human joints." pp. 1006409-1.
[33] J. Kim, M.-H. Kim, K. Job, J. Hab, Y. Kim, D.-J. Lim, C. Kim, Photoacoustic analysis of thyroid cancer in vivo: a pilot study, SPIE Photons Plus Ultrasound: Imaging and Sensing, San Francisco, California, United States (2017) pp. 1006408.
[34] P.J. van den Berg, R. Bansal, K. Daoudi, W. Steenbergen, J. Prakash, Preclinical detection of liver fibrosis using dual-modality photoacoustic/ultrasound system, Biomed. Opt. Express 7 (12) (2016) 5081–5091.
[35] M.K.A. Singh, W. Steenbergen, Photoacoustic-guided focused ultrasound (PAFUSion) for identifying reflection artifacts in photoacoustic imaging, Photoacoustics 3 (4) (2015) 123–131.
[36] J. Xia, C. Huang, K. Maslov, M.A. Anastasio, L.V. Wang, Enhancement of photoacoustic tomography by ultrasonic computed tomography based on optical excitation of elements of a full-ring transducer array, Opt. Lett. 38 (16) (2013) 3140–3143.
[37] J. Jose, R.G. Willemink, W. Steenbergen, C.H. Slump, T.G. van Leeuwen, S. Manohar, Speed-of-sound compensated photoacoustic tomography for accurate imaging, Med. Phys. 39 (12) (2012) 7262–7271.
[38] X.L. Dean-Ben, V. Ntziachristos, D. Razansky, Acceleration of optoacoustic model-based reconstruction using angular image discretization, IEEE Trans. Med. Imaging 31 (5) (2012) 1154–1162.
[39] M. Xu, L.V. Wang, Universal back-projection algorithm for photoacoustic computed tomography, Phys. Rev. E 71 (1) (2005) pp. 016706.
[40] K.P. Köstli, M. Frenz, H. Bebie, H.P. Weber, Temporal backward projection of optoacoustic pressure transients using Fourier transform methods, Phys. Med. Biol. 46 (7) (2001) 1863.
[41] A. Rosenthal, D. Razansky, V. Ntziachristos, Fast semi-analytical model-based acoustic inversion for quantitative optoacoustic tomography, IEEE Trans. Med. Imaging 29 (6) (2010) 1275–1285.
[42] X.L. Deán-Ben, V. Ntziachristos, D. Razansky, Acceleration of optoacoustic model-based reconstruction using angular image discretization, IEEE Trans. Med. Imaging 31 (5) (2012) 1154–1162.
[43] P.C. Hansen, Analysis of discrete ill-posed problems by means of the L-curve, Siam Rev. 34 (4) (1992) 561–580.
[44] P.K. Yalavarthy, B.W. Pogue, H. Dehghani, K.D. Paulsen, Weight-matrix structured regularization provides optimal generalized least-squares estimate in diffuse optical tomography, Med. Phys. 34 (6Part1) (2007) 2085–2098.
[45] P.K. Yalavarthy, B.W. Pogue, H. Dehghani, C.M. Carpenter, S. Jiang, K.D. Paulsen, Structural information within regularization matrices improves near infrared diffuse optical tomography, Opt. Express 15 (13) (2007) 8043–8058.
[46] Y. Han, S. Tzoumas, A. Nunes, V. Ntziachristos, A. Rosenthal, Sparsity-based acoustic inversion in cross-sectional multiscale optoacoustic imaging, Med. Phys. 42 (9) (2015) 5444–5452.
[47] A.C. Bovik, Handbook of Image and Video Processing, Academic press, 2010.
[48] D. Hyde, E.L. Miller, D.H. Brooks, V. Ntziachristos, Data specific spatially varying regularization for multimodal fluorescence molecular tomography, IEEE Trans. Med. Imaging 29 (2) (2010) 365–374.
[49] A. Dima, V. Ntziachristos, In-vivo handheld optoacoustic tomography of the human thyroid, Photoacoustics 4 (2) (2016) 65–69.
[50] A. Buehler, M. Kacprowicz, A. Taruttis, V. Ntziachristos, Real-time handheld multispectral optoacoustic imaging, Opt. Lett. 38 (9) (2013) 1404–1406.
[51] J.P. Peruga, J.Z. Peruga, J.D. Kasprzak, R. Kręcki, Ł. Jankowski, P. Zając, M. Plewka, Ultrasound evaluation of forearm arteries in patients undergoing percutaneous coronary intervention via radial artery access: results of one-year follow-up, Kardiologia Polska (Polish Heart Journal) 73 (7) (2015) 502–510.
[52] M.W. Lorenz, H.S. Markus, M.L. Bots, M. Rosvall, M. Sitzer, Prediction of clinical cardiovascular events with carotid intima-media thickness: a systematic review and meta-analysis, Circulation 115 (4) (2007) 459–467.
[53] S.L. Jacques, Optical properties of biological tissues: a review, Phys. Med. Biol. 58 (11) (2013) R37.
[54] F. Timischl, The contrast-to-noise ratio for image quality evaluation in scanning electron microscopy, Scanning 37 (1) (2015) 54–62.
[55] Z. Wang, A.C. Bovik, H.R. Sheikh, E.P. Simoncelli, Image quality assessment: from error visibility to structural similarity, IEEE Trans. Image Process. 13 (4) (2004) 600–612.
[56] T. Abe, Genesis 49 (2011) 579–590.
[57] P. E. Kinahan, B. H. Hasegawa, and T. Beyer, "X-ray-based attenuation correction for positron emission tomography/computed tomography scanners." pp. 166-179.
[58] R.P. Woods, J.C. Mazziotta, S.R. Cherry, MRI-PET registration with automated algorithm, J. Comput. Assist. Tomogr. 17 (4) (1993) 536–546.
[59] A. Ale, V. Ermolayev, E. Herzog, C. Cohrs, M.H. De Angelis, V. Ntziachristos, FMT-XCT: in vivo animal studies with hybrid fluorescence molecular tomography-X-ray computed tomography, Nat. Methods 9 (6) (2012) 615–620.
[60] R.B. Schulz, A. Ale, A. Sarantopoulos, M. Freyer, E. Soehngen, M. Zientkowska, V. Ntziachristos, Hybrid system for simultaneous fluorescence and x-ray computed tomography, IEEE Trans. Med. Imaging 29 (2) (2010) 465–473.
[61] J. Prakash, P.K. Yalavarthy, Data-resolution based optimal choice of minimum required measurements for image-guided diffuse optical tomography, Opt. Lett. 38 (2) (2013) 88–90.
[62] X. Ren, J. Malik, Learning a classification model for segmentation, IEEE International Conference on Computer Vision, Nice, France, France, 2003, pp. 10–17.
[63] S. Ramani, Z. Liu, J. Rosen, J.-F. Nielsen, J.A. Fessler, Regularization parameter selection for nonlinear iterative image restoration and MRI reconstruction using GCV and SURE-based methods, IEEE Trans. Image Process. 21 (8) (2012) 3659–3672.

Hong Yang is a Ph.D. student in the Institute for Biological and Medical Imaging (IBMI) at Technische Universität **München** and Helmholtz Zentrum München, Germany. She received MEng in Optical Engineering from Xidian University, China. Her current research interests are in biomedical imaging, signal processing and inverse problems.

Dominik Jüstel studied mathematics and informatics at the Technical University of Munich (TUM), graduating at the Chair for Mathematical Modeling of Biological Systems in association with the Institute for Biomathematics and Biometry at the Helmholtz Center Munich. He received his doctoral degree (Dr. rer. nat.) in mathematics with highest distinction at the Chair for Analysis at TUM. After a postdoc at the mathematics faculty of TUM, Dr. Jüstel joined the Chair for Biological Imaging at TUM and the Institute for Biological and Medical Imaging at the Helmholtz Center Munich. With his group for Computation & Analytics at TranslaTUM, he works on quantitative multispectral optoacoustic tomography and advanced data analysis for various optical and optoacoustic imaging modalities.

Jaya Prakash obtained M.Sc. in computational sciences and Ph.D. in optical image reconstructions/inverse problems in 2012 and 2014 respectively. Later, he moved to Munich as a Group Leader and Alexander von Humboldt Fellow at the Institute for Biological and Medical Imaging (IBMI), Helmholtz Zentrum München and at the Chair for Biological Imaging, Technical University Munich, where he had worked till 2018. He has been working in the Department of Instrumentation and Applied Physics, IISc as an Assistant Professor since 2019.

Angelos Karlas studied Medicine (M.D.) and Electrical and Computer Engineering (Dipl.-Ing.) at the Aristotle University of Thessaloniki, Greece. He holds a Master of Science in Medical Informatics (M.Sc.) from the same university and a Master of Research (M.Res.) in Medical Robotics and Image-Guided Intervention from Imperial College London, UK. He is currently working as clinical resident at the Department for Vascular and Endovascular Surgery at the Rechts der Isar University Hospital in Munich, Germany. He is also the Group Leader of the interdisciplinary Clinical Bioengineering Group at the Helmholtz Center Munich, Germany while pursuing his Ph.D. (Dr.rer.nat.) in Experimental Medicine at the Technical University of Munich, Germany. In the past, he served as the Clinical Translation Manager at the Institute for Biological and Medical Imaging of the Helmholtz Center Munich, Germany as well as the Junior Group Leader of the Clinical Translation Group at the same institute. His research interests are in the areas of innovative vascular and metabolic imaging and image-guided vascular interventions.

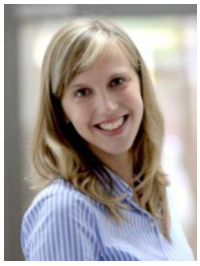

Anne Helfen is a radiologist at the at the Institute of Clinical Radiology of the University Hospital Muenster/Germany. She studied medicine in Muenster/Germany, Zurich/Switzerland and London/UK and received her MD degree at the University of Muenster. Her research interests are molecular and translational imaging of tumor immune interaction.

Max Masthoff is currently a resident for Radiology at the University Hospital of Muenster and postdoc researcher at the Translational Research Imaging Centre (TRIC) at the University of Muenster. He received his MD at the University of Muenster. His current research interest is translational photacoustic imaging of vascular and oncologic diseases.

Professor Moritz Wildgruber attended Medical School in Hamburg and Munich. After receiving is MD he completed a postdoctoral research fellowship at the Center for Molecular Imaging Research at Massachusetts General Hospital/Harvard Medical School, with the focus on investigating immune cell function in cardiovascular diseases. Following his post-do he completed his Radiology residency at the Klinikum rechts der Isar of the TU Munich and further subspecialized in Interventional Radiology. Currently he is Professor for Radiology at the University Hospital of Münster an heads a research group in molecular imaging focused on the translation of novel imaging techniques into clinical practice.

Professor Vasilis Ntziachristos studied Electrical Engineering at Aristotle University in Thessaloniki, Greece and received his M.Sc. and Ph.D. from the Bioengineering Department of the University of Pennsylvania. He served as assistant professor and director of the Laboratory for Bio-Optics and Molecular Imaging at Harvard University and Massachusetts General Hospital. Currently, he is the Director of the Institute for Biological and Medical Imaging at the Helmholtz Zentrum in Munich, Germany, as well as a Professor of Electrical Engineering, Professor of Medicine and Chair for Biological Imaging at the Technical University Munich, Germany. His work focuses on novel innovative optical and optoacoustic imaging modalities for studying biological processes and diseases as well as the translation of these findings into the clinic.